Investigation of Zn and Cu prepulse plasmas relevant to collisional excitation x-ray lasers

B. Rus,[1] P. Zeitoun,[2,3] T. Mocek,[1] S. Sebban,[2] M. Kálal,[4] A. Demir,[3,*] G. Jamelot,[2] A. Klisnick,[2] B. Králiková,[1] J. Skála,[1] and G. J. Tallents[3]

[1]*Gas Lasers Department, Institute of Physics, 18040 Prague 8, Czech Republic*

[2]*Laboratoire de Spectroscopie Atomique et Ionique, Bâtiment 350, Université de Paris–Sud, 91405 Orsay Cedex, France*

[3]*Department of Physics, University of Essex, Colchester CO4 3SQ, United Kingdom*

[4]*Faculty of Nuclear Sciences and Physical Engineering, Czech Technical University, 11519 Prague 1, Czech Republic*

(Received 7 May 1997)

This paper presents the results of a comparative experimental study of low-temperature Zn and Cu line plasmas created on slab targets by 400-ps laser pulse producing irradiance from 4×10^{9} to 10^{11} W cm^{-2}. The aim was to examine the nanosecond-scale postpulse evolution of plasmas created in conditions equivalent to those produced by prepulses in collisional x-ray lasers, of elements that have neighboring atomic numbers but very different material properties. The plasmas were interferometrically probed at 4 and 10 ns next to the driving pulse, using geometry that made it possible to obtain an authentic two-dimensional (2D) electron density pattern in the plane perpendicular to the plasma axis. VIS-IR spectroscopy and imaging were used to provide an indication of the electron temperature and volume of the plasma layer near the target. We observe that over the whole range of the applied irradiances the characteristics and/or the expansion history of the Zn and Cu plasmas are very different. For irradiance exceeding a threshold specific to each element the density patterns exhibit an unexpected structure characterized by symmetrical flanks strongly localized in space, suggesting plasma is generated in addition to that produced within the laser pulse duration. The results imply that during the postpulse time the energy coupling between the plasma and the target is substantial for the plasma flow that exhibits a complex 2D character. A comparison of the data and results of a 1.5D hydrodynamic simulation for 10^{11} W cm^{-2} is made, indicating reasons for problems of such models in the treatment of the plasmas in question, and thus in the treatment of small-prepulse action in some x-ray laser systems. [S1050-2947(97)07011-X]

PACS number(s): 42.55.Vc, 52.50.Jm, 52.70.−m, 79.20.Ds

I. INTRODUCTION

The performance of soft-x-ray lasers using collisional pumping has been dramatically improved over the past a few years [1,2]. The progress in development of these devices has been especially fostered by using sequential pumping in which a succession of two or several pulses of different intensity are employed to create plasma with appropriate conditions for driving population inversion and for propagation of the x-ray beam. The concept of multipulse pumping has been experimentally implemented in several modifications, such as the use of a weak single or multiple prepulse applied several ns ahead of the main pulse of subnanosecond duration [3–6]. Another possibility involves the application of a sequence of two or three typically 100-ps pulses of comparable intensity and separated by several hundred ps [7,8], a third combines a nanosecond background with a high-intensity picosecond pulse [9,10]. While the latter approach is still in an early state of development, the first two arrangements have demonstrated saturated and nearly monochromatic output at 18.2, 19.6, 21.2, and 25.5 nm in Ne-like selenium, germanium, zinc, and iron, respectively [11–15] and at 14 nm in Ni-like silver [16]. By applying these techniques amplification has been further demonstrated over a wide range of low- and medium-Z elements using both Ne-like [17,18] and Ni-like [19–21] isoelectronic systems.

Given the prospect of the prepulse or multipulse pumping to ultimately approach the full design potential of the collisional soft x-ray systems, some lasers were studied in detail, both theoretically and experimentally (see, e.g., [22–30]). The study reveals that for systems using a typical double-pulse configuration or prepulses comparable to or in excess of $\approx10^{12}$ W cm^{-2} (typically up to $\sim$10% of the main pulse) there is generally good agreement between the simulations and the experiments. However, for systems involving prepulses producing less than 10^{12} W cm^{-2} and/or large delays—typically several ns—between the individual features in the sequence, the current hydrodynamic and atomic kinetics models employing 1.5D geometry are incapable of explaining the sensitivity to weak prepulses, even when including a treatment of target solid-state properties. Nevertheless, using prepulses at a level of 10^{10} W cm^{-2} or weaker was revealed to be very efficient in a number of medium-Z lasers such as Cr, Zn, and Ge [4–6,14,18], and is also relevant to combined ns-ps driving [31,32] as well as to optical-field-ionization systems [33]. On the whole, understanding of the evolution of plasmas created by an irradiance below $\approx10^{12}$ W cm^{-2} is presently rather insufficient, especially in regard to the period after the termination of the laser pulse.

A recent systematic study of the prepulse effect on amplification in Ne-like Zn ($Z=30$), Cu ($Z=29$), and Ni ($Z=28$) plasmas created from a slab target at a fixed intensity of the main pulse [34] revealed significantly different behavior with respect to the prepulse intensity and delay. By em-

*Present address: Department of Physics, University of Kocaeli, Izmit 41100, Turkey.

TABLE I. Solid-state properties of copper ($Z=29$) and zinc ($Z=30$) (compiled from Refs. [35–37]).

		Cu	Zn
Electron conductivity	($m\Omega^{-1}$)	5.92×10^{7}	1.67×10^{7}
Skin depth (1.315 μm laser)	(nm)	2.1	4.1
Solid density (at 25 °C)	($g\ cm^{-3}$)	8.96	7.14
Specific heat capacity	($J\ g^{-1}\ K^{-1}$)	3.85×10^{-1}	3.88×10^{-1}
Thermal conductivity of solid (at 25 °C)	($W\ cm^{-1}\ K^{-1}$)	4.01	1.16
Melting point	(°C)	1085	420
Latent fusion heat	($kJ\ mol^{-1}$)	13.1	7.41
Thermal conductivity of liquid (near the melting point)	($W\ cm^{-1}\ K^{-1}$)	1.60	0.59
Boiling point	(°C)	2563	907
Latent vaporization heat	($kJ\ mol^{-1}$)	304.6	115.3
1^{st} ionization potential	(eV)	7.73	9.40
2^{nd} ionization potential	(eV)	20.30	17.99
3^{rd} ionization potential	(eV)	36.87	39.75

ploying prepulses of an intensity ranging from $\sim10^{8}$ to $\sim10^{12}$ W cm^{-2}, applied 2 or 4.5 ns ahead of the main pulse, Zn and Ni exhibited much larger enhancement than Cu of amplification at the transition of concern $(2p_{1/2}3p_{1/2})_{J=0}\rightarrow(2p_{1/2}3s_{1/2})_{J=1}$, though all three elements benefited from the longer prepulse delay. Moreover, the amplification in Zn was found to be maximized for a prepulse producing $\approx2\times10^{10}$ W cm^{-2}, in strong contrast to Cu and Ni, exhibiting increasing output with the prepulse level. While plasma hydrodynamics and atomic kinetics relevant to the main pulse are assumed to be similar for such Z-neighbouring lasers, the stark differences in their sensitivity to a prepulse throughout the *whole* examined range of intensities (i.e., up to 10^{12} W cm^{-2}) must occur due to different features of the prepulse plasmas into which the main pulse is subsequently coupled.

The goal of the current work was to provide a detailed experimental characterization of line plasmas generated from slab targets by irradiances equivalent to those produced by low-intensity prepulses in some collisional x-ray lasers, with the prospect of offering a testing ground for numerical simulations used to model such systems. The experiment was carried out as a comparative study of Zn ($Z=30$) and Cu ($Z=29$) plasmas created by irradiance ranging from 4×10^{9} to 10^{11} W cm^{-2}, and of their expansion over 10 ns following the laser pulse. Hence for both targets the following parameters were examined: (i) electron density outline in the plane perpendicular to the plasma axis, 4 and 10 ns subsequent to the laser pulse, (ii) VIS-IR time-integrated spectrum emitted by the plasma, and (iii) spatially resolved plasma emission profile in the VIS-IR spectral region.

Selected properties of Cu and Zn relevant to plasma generation by low and moderate irradiance are shown in Table I. It is seen that through solid, liquid, and gaseous states their thermal characteristics strongly differ—most notably, both latent heats of phase transitions and the melting and boiling points of Cu are 2–3 times higher than in Zn, which implies that for Cu much larger energy is needed to bring a unity of the solid onto the ionization threshold. In addition, the more than 3 times larger thermal conductivity of Cu suggests a more significant transfer of energy from the plasma into the solid target compared to Zn.

The organization of this paper is as follows. In Sec. II we present details of the experimental setup and briefly describe principles used in the data analysis. In Sec. III the obtained results are shown. Implications on the physics of the investigated plasmas are outlined in Sec. IV. Also, the electron density profiles obtained for Zn at the irradiance 10^{11} W cm^{-2}, where solid-state effects are presumed to be insignificant during the laser pulse, are compared to results of the numerical modeling using a standard 1.5D hydrocode. Conclusions are presented in Sec. V.

II. EXPERIMENTAL ARRANGEMENT

The target configuration and the arrangement of the employed diagnostics are illustrated in Fig. 1. The investigated line plasmas were generated by irradiating Zn and Cu slab targets 1 mm wide by near Gaussian $\sim$400-ps full width at half maximum (FWHM) pulses of the iodine laser system PERUN at the Institute of Physics, at the fundamental wavelength 1.315 μm. To produce nearly perfect irradiation uniformity in the longitudinal direction, the 75-mm-in-diameter laser beam was focused solely in the vertical direction down to a 100($\pm$10)-μm-wide line, and just a small central fraction of the focus length was used to drive the plasma. Net target irradiances equal to 4×10^{9}, 10^{10}, 2×10^{10}, 5×10^{10}, and 10^{11} W cm^{-2} were produced by using variously reflective mirrors or semi-transparent plates as the relay device directing the beam towards the chamber—the beam, and hence the focus, profile was thus identical for all the irradiances applied. The energy of the beam entering the chamber was carefully measured, and the given values of net irradiance are estimated to be precise within $\pm20\%$.

Interferometric probing was used to determine the electron density pattern in the plane perpendicular to the plasma axis, in instants 4 and 10 ns following the peak of the driving pulse. For this purpose a fraction of the 1.315-μm beam was extracted from the laser output and frequency tripled in DKDP crystals to provide 438-nm emission, which was sent, via a delay line, to illuminate the plasma down its axis (for

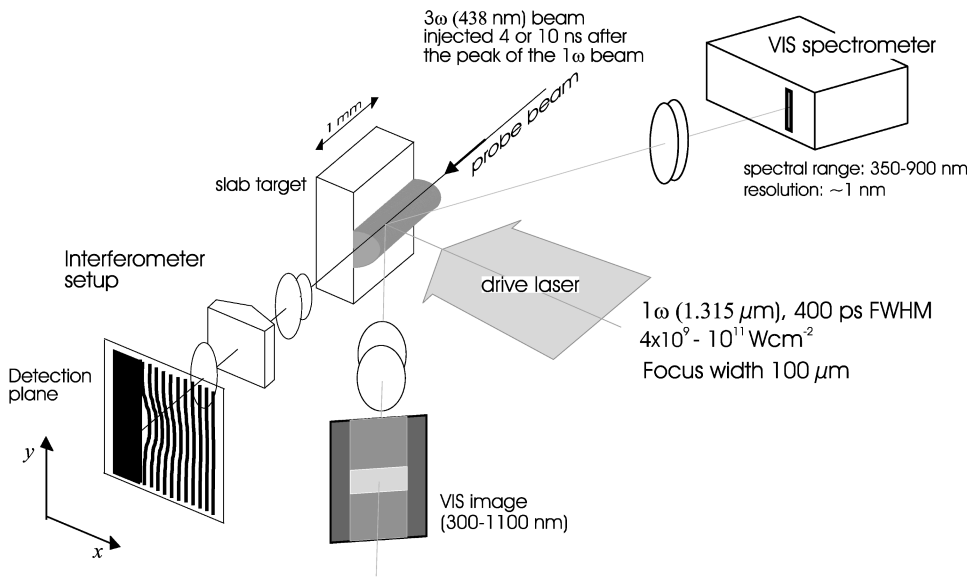

FIG. 1. Experimental setup. The investigated 1-mm-long line plasma is created by the 1.315-μm fundamental beam of an iodine laser, and is probed by the third harmonics beam at 438.3 nm. High irradiation uniformity is ensured by using only a small fraction of the line-focused (100 μm$\times$75 mm) 1.315-μm beam—most of the laser energy is deliberately dumped.

details see [38]). An additional spatial filter was employed in the optical path of this probe beam so as to improve its optical quality and to reduce its diameter down to $\sim$5 mm, a value sufficient to largely overfill the plasma. Care was taken to precisely align the target surface parallel to the probe beam. The interferometric patterns were produced by a Nomarski-type setup. A Fresnel biprism was used to recombine the phase-delayed part of the probe beam that had passed through the plasma, and the part that had passed in free space far away from the target. A microscope objective and a lens ensured imaging of the plasma output plane on the detector, with a magnification $\sim$16.5. The interferograms were recorded by a 16-bit 375$\times$242 pixel charge-coupled device (CCD) camera, cooled down to $-15\,^{\circ}$C.

The 438-nm probe beam can potentially access electron densities up to the critical value $n_{ce}=5.7\times10^{21}$ cm^{-3}, however, refraction in the steep-gradient plasma near the target substantially reduces this value. Based on a simple computer modeling, the choice of the target length of 1 mm stemmed from the requirement to keep the refraction effects acceptable in the plasma corona while still allowing the production of plasmas with a sufficient aspect ratio, so that boundary effects do not impair the precision of the experiment.

The adopted geometry allows one to obtain the *authentic* electron density profile in the plane perpendicular to the plasma axis. Assuming the refraction of the probe beam to be negligible, the electron density along a sampling ray is constant and hence there is no need to analyze the data by using a recurrence scheme such as Abel inversion, imposing arbitrary assumptions on the density symmetry. The electron density n_e in a point (x,y) may be thus inferred from the difference ϕ between the optical path length along a ray propagated in free space and the path length along the ray passing through this point

$$\phi(x,y)=\frac{2\pi}{\lambda}\,l\left[1-\left(1-\frac{n_e(x,y)}{n_{ce}}\right)^{1/2}\right]\cong\frac{\pi}{\lambda}\,\frac{n_e(x,y)}{n_{ce}}\,l, \tag{1}$$

where λ is the wavelength of the probe beam, l the plasma length, and $n_e\ll n_{ce}$ is assumed. Using this relationship and characterizing the fringe pattern in terms of normalized shift $\phi(x,y)=\phi(x,y)/2\pi$ (so that shift of a fringe by one period corresponds to $\phi=1$), it is

$$n_e(x,y)=\frac{2n_{ce}\lambda}{l}\,\overline{\phi}(x,y). \tag{2}$$

The majority of interferograms obtained in this work was analyzed with the help of this relationship, i.e., the fringe patterns were first transformed into a ''map'' of shifts of individual fringes, which was then converted into the contour lines of electron density. Other interferograms, especially those corresponding to an only marginally perturbed fringe pattern, were analyzed by using a fast Fourier transform technique. Its basic idea [39] is based on unfolding the function $\phi(x,y)$ by bandpassing the frequency spectrum of the interferogram, while the result is subsequently phase detected in the space domain. More specifically, the carrier frequency ω corresponding to unperturbed fringes is rejected from the spectrum of the pattern function $\cos\{\omega x+\phi(x,y)\}$, and the density is inferred from the filtered function $\cos\{\phi(x,y)\}$ by using the relationship from Eq. (1). The method is analogous to demodulation and phase detection used in FM systems in communication technique; its implementation, however, requires an appropriate treatment for $\phi>\pi$, which is discussed in Ref. [39].

The array of employed diagnostics further included a spectrometer and an imaging system, both working in the visible or near-infrared region. The plasma line emission was spectrally analyzed using a Czerny-Turner setup, providing a space- and time-integrated spectrum from approximately 350 to 900 nm. The emission was imaged with a magnification of $\sim$0.5 by a lens doublet onto the entrance slit of a spectrometer incorporating a blazed lithographic grating with period of 280 nm, and two spherical mirrors. The spectra were re-

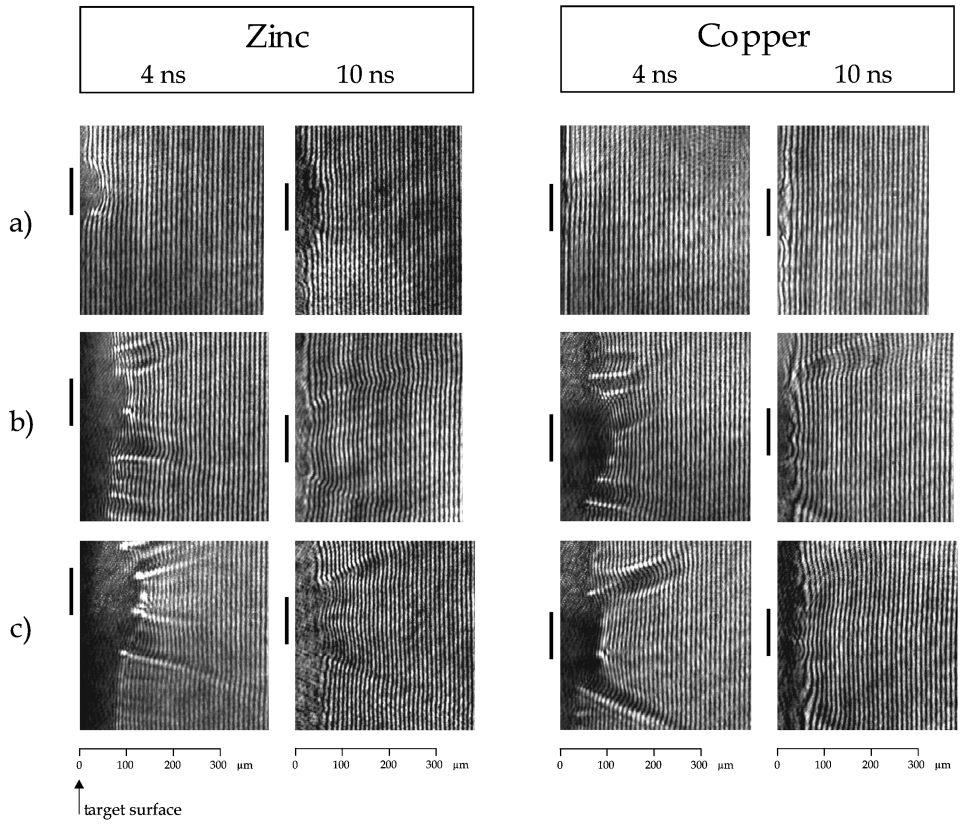

FIG. 2. Typical interferometric patterns obtained in $t=4$ ns and $t=10$ ns for plasmas generated by (a) 10^{10}, (b) 5×10^{10}, and (c) 10^{11} W cm^{-2}. The vertical bar labels the width ($=100$ μm) and the position of the laser impact for each shot. The left end of the records corresponds to the target surface, with an accuracy of ±5 μm. Access to higher electron densities near the target is hampered by refraction of the probe beam.

corded by a 512-pixel linear CCD of calibrated spectral response. The setup provides resolving power $\lambda/\Delta\lambda$ of ≈500 and enables one to distinguish spectral features separated by ~1 nm.

The electron temperature was inferred from the spectra by using local thermodynamic equilibrium (LTE) approach. The criterion for LTE is that the population kinetics of a given set of levels separated by ΔE must be dominated by collisional processes (i.e., the contribution of radiative processes is negligible), which occurs [40] for the electron density n_e (in cm^{-3}),

$$n_e \geqslant 1.8\times10^{14} T_e^{1/2} \Delta E^3, \tag{3}$$

where the electron temperature T_e and ΔE are expressed in eV. Regarding the results of the interferometric probing evidenced for the investigated plasmas electron densities superior to $\sim10^{18}$ cm^{-3}, spectral lines of wavelength $\lambda_{[\mathrm{nm}]} \geqslant 70 T_e^{1/6}$ are appropriate for this diagnostics. The electron temperature is then determined from the relationship for the intensity ratio I_2/I_1 of two lines belonging to the same ionization state:

$$\frac{I_2}{I_1} = \frac{A_2}{A_1}\frac{\lambda_1}{\lambda_2}\frac{g_2}{g_1}\exp\left(-\frac{E_{2u}-E_{1u}}{kT_e}\right), \tag{4}$$

where A_1,λ_1,g_1,E_{1u} and A_2,λ_2,g_2,E_{2u} are, respectively, the spontaneous emission probabilities, the wavelengths, the statistical weights, and the energies of the upper levels for each transition.

The optical imaging was carried out with the help of a telescope providing a magnification of ~3, coupled with a high-resolution 192×165-pixel CCD camera. As outlined in Fig. 1, it viewed the plasma under an angle of 60° with respect to the target normal. The recorded signal corresponds to the range $\sim300-1100$ nm given by the throughput of the used optics and by the CCD spectral sensitivity. The system is used to provide the lateral profile of the VIS-IR emission, besides verifying the plasma uniformity down its axis. Advantage was taken of the insensitivity of the CCD to radiation of a wavelength beyond ~1.2 μm, hence no cutoff filtering was necessary to eliminate the scattered 1.315-μm laser light.

III. RESULTS

Both Zn and Cu plasmas were investigated in two identical series of shots involving for each of the available irradiances (4×10^9, 10^{10}, 2×10^{10}, 5×10^{10}, and 10^{11} W cm^{-2}) probing in times $t=4$ and 10 ns after the peak of the driving pulse. For each combination of these experimental parameters at least two shots were carried out so as to establish the reproducibility of the data and to verify that these are not subject to microscopic variations of the quality of the target

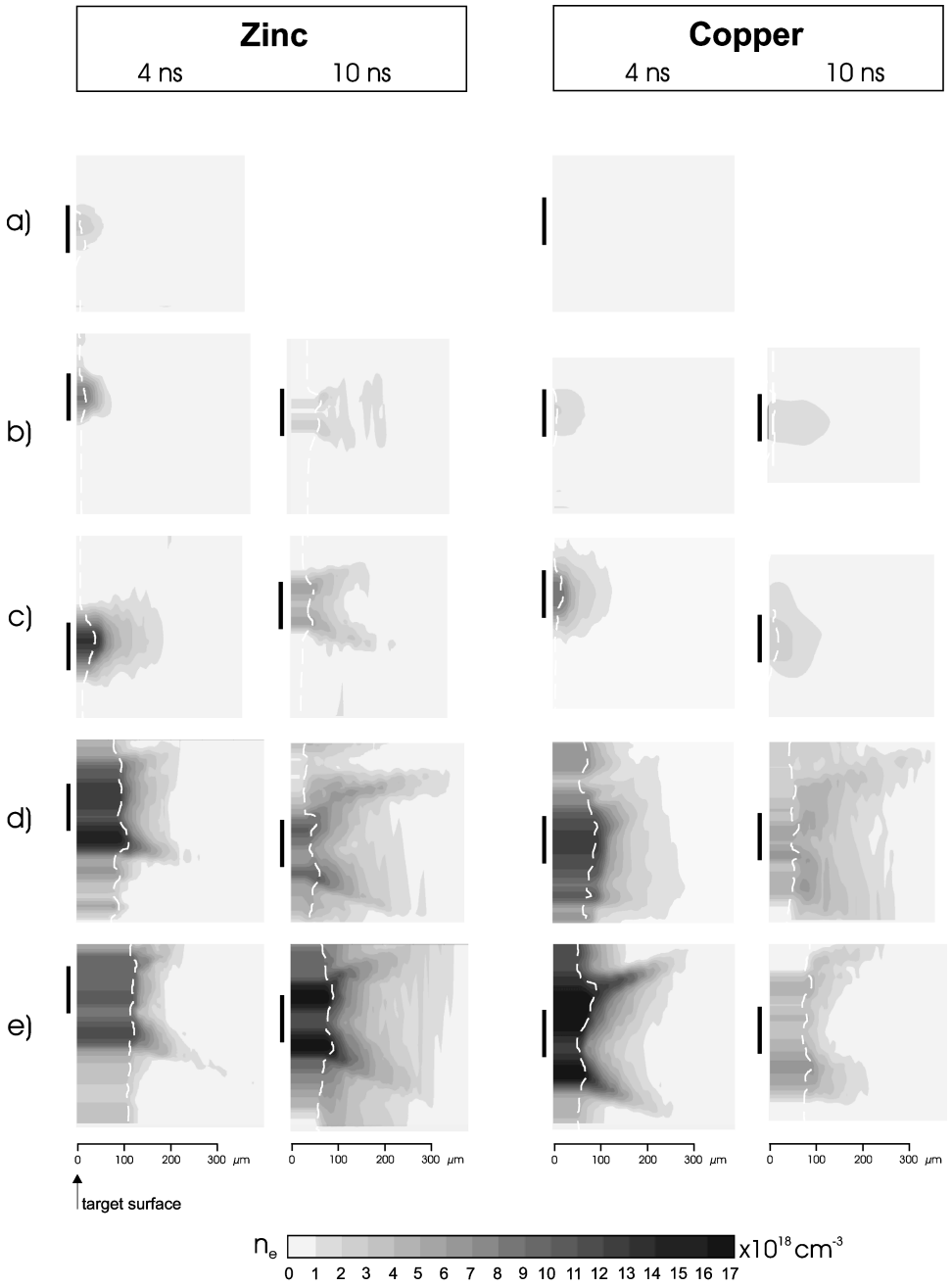

FIG. 3. Electron density distribution of plasmas created by (a) 4×10^9, (b) 10^{10}, (c) 2×10^{10}, (d) 5×10^{10}, and (e) 10^{11} W cm^{-2}, obtained by unfolding the corresponding interferograms including those from Fig. 2. The vertical bar indicates the width ($=100$ μm) and the position of the laser impact for each shot, and the left end of the images corresponds to the position of the target surface. The dotted lines indicate the limit of the fringe pattern providing relevant density data (see text).

surface, especially for the lowest irradiances.

A. Profiles of the electron density

A sample of the raw interferometric data is shown in Fig. 2. They clearly illustrate the characteristic features of the plasma density pattern throughout the investigated irradiance interval. It may first be seen that while for low irradiances the plasma is rather localized near the target surface and laterally limited to the 100-μm width of the laser focus, for irradiances equal to, or in excess of, 5×10^{10} W cm^{-2} the interferograms show evidence of plasmas of a ''nozzlelike'' profile. It should be mentioned that the patterns exhibit excellent shot-to-shot reproducibility for $t=10$ ns, and only minor fluctuations for $t=4$ ns. The second apparent feature is the difference between Zn and Cu throughout the investigated range of irradiances. This is obvious both from the interferograms corresponding to 10^{10} W cm^{-2}, which reveal significantly denser and more spread-out plasma in the case of Zn, and also for 5×10^{10} and 10^{11} W cm^{-2} where Cu provides plasma that in the lateral direction are appreciably larger than in the case of Zn.

A full account of the obtained results is displayed in Fig. 3 (the density profiles corresponding to 4×10^9 W cm^{-2} and $t=10$ ns are not available as the interferograms are corrupted

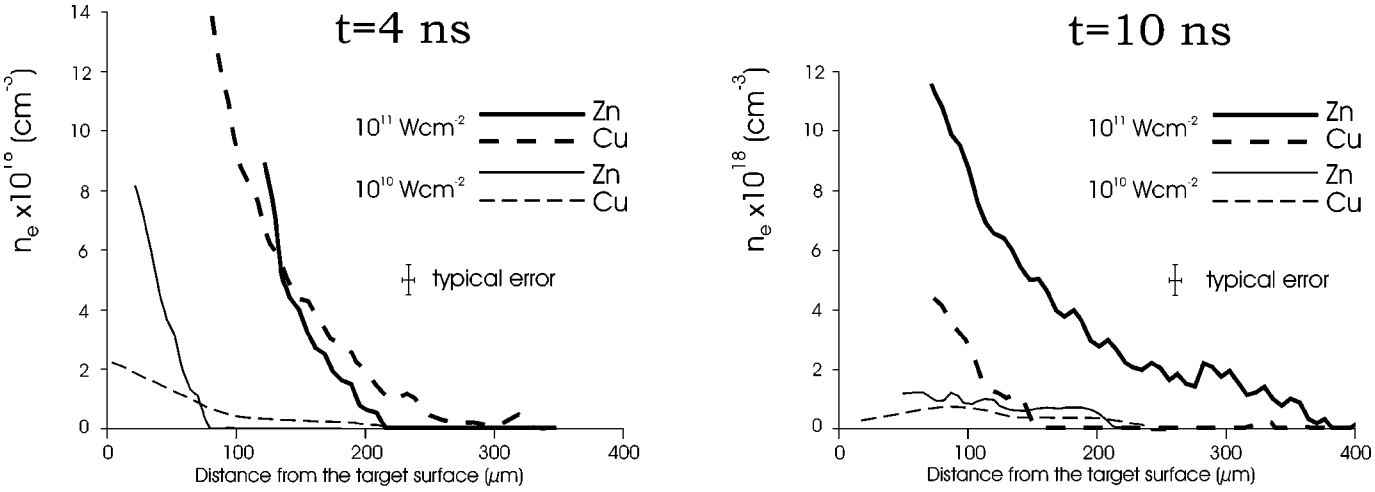

FIG. 4. Electron density profiles of Zn (solid line) and Cu (dashed line) plasmas created by 10^{10} and 10^{11} W cm^{-2}, corresponding to the center of the laser focus. The $t=4$ ns profiles reveal that plasmas of comparable but slightly higher local density are generated in the case of Zn, while the $t=10$ ns profiles indicate strongly different decay rates of Zn and Cu plasmas.

due to refraction of the probe beam). The high-density plasma adjacent to the target surface, inaccessible due to refraction and/or blur of the interference fringes, is represented for clarity by a gray level corresponding to that inferred from the last discernible fringe, and is delimited by the dotted line. From the results corresponding to $t=4$ ns it is seen that as the irradiance is lower than or equal to 2×10^{10} W cm^{-2}, both Zn and Cu plasmas exhibit a pattern pertinent to an expanded layer, with a lateral size approximately equal to the focus width. This indicates that the plasma expansion up to 4 ns is near to planar and its character is governed by the energy distribution imposed by the laser, inasmuch as the peak electron density in the lateral direction corresponds to the axis of the focus. The density patterns of the Zn and Cu plasmas are similar in shape, though significantly higher electron densities are generated using Zn targets.

As the irradiance exceeds 5×10^{10} W cm^{-2}, the character of the $t=4$ ns profiles dramatically changes. A ''nozzlelike'' structure with a density dip in the center appears, exhibiting symmetrical and strongly localized density flanks. The angle of these flanks with respect to the target normal of about 20–25 degrees is essentially independent both of the target and of the irradiance. In contrast, there is a difference between the Zn and Cu plasmas in lateral width, the latter exhibiting, for a given distance x from the surface, a larger span between the flanks. By extrapolating the direction of the flanks towards the surface, one finds that in the case of Zn they outline a 100–120-μm-wide region, while for Cu they correspond to an area of 120–160 μm. Besides the principal flank structure the data also reveal small filamentary streams emanating from the surface far off the impact region—however, these features rather absorb the probe radiation while exhibiting only a low electron density.

Another characteristic of the $t=4$ ns data corresponding to high irradiances is, for both Zn and Cu, a thick surface layer refracting and/or absorbing the probe 438-nm radiation and extending over a large distance away from the laser-driven area—on the interferometric records it appears nearly uniform over the $\sim$400-μm viewed height. The exact thickness of this ''dark region'' fluctuates between 80 and 150 μm on a shot-to-shot basis; however, it is always present in the shots carried out at 5×10^{10} and 10^{11} W cm^{-2}, in contrast to the $t=4$ ns data obtained at lower irradiances.

The $t=10$ ns density snapshots allow one to obtain a fuller understanding of some processes involved in the plasma expansion, as well as reasons for the differences between Zn and Cu. The first outstanding feature is the strongly different ways in which the Zn and Cu plasmas created by 10^{10} and 2×10^{10} W cm^{-2} evolve from a localized plasma layer existing in early times. The Cu plasmas decay principally by expanding away from the target surface and the density patterns imply a presumably adiabatic flow regime of a plasma layer created beforehand, and assisted by cooling through contact with the target. In contrast, the qualitative change of the profiles of the Zn plasmas from 4 to 10 ns, namely, the formation of the two spatially localized high-density flanks, evidently cannot arise as a result of the expansion of an already existing plasma. This suggests that additional plasma is generated during this period while its bulk is expelled obliquely with respect to the target surface and supplies the density flanks.

While for 5×10^{10} and 10^{11} W cm^{-2} both the Zn and Cu plasmas exhibit the nozzlelike profile as early as in $t=4$ ns, Figs. 3(d) and 3(e) corresponding to $t=10$ ns reveal the ensuing evolution of these plasmas to be different. The profiles show that while for Zn the flank structure is enhanced between $t=4$ and 10 ns, suggesting ongoing plasma generation near the target, the Cu plasma rather decays in density and the flanks ''wash out'' in space.

Figure 4 shows the electron density distribution along a slice corresponding to the center of the laser impact for irradiances 10^{10} and 10^{11} W cm^{-2}. First, the $t=4$ ns profiles reveal that throughout the investigated interval of irradiances the Zn target provides plasma of a higher local density and of a larger density gradient. Secondly, the $t=10$ ns data reveal that the density of the Cu plasmas decreases in time at a higher rate, which is especially evident by comparing the $t=4$ and 10 ns profiles corresponding to 10^{11} W cm^{-2} and

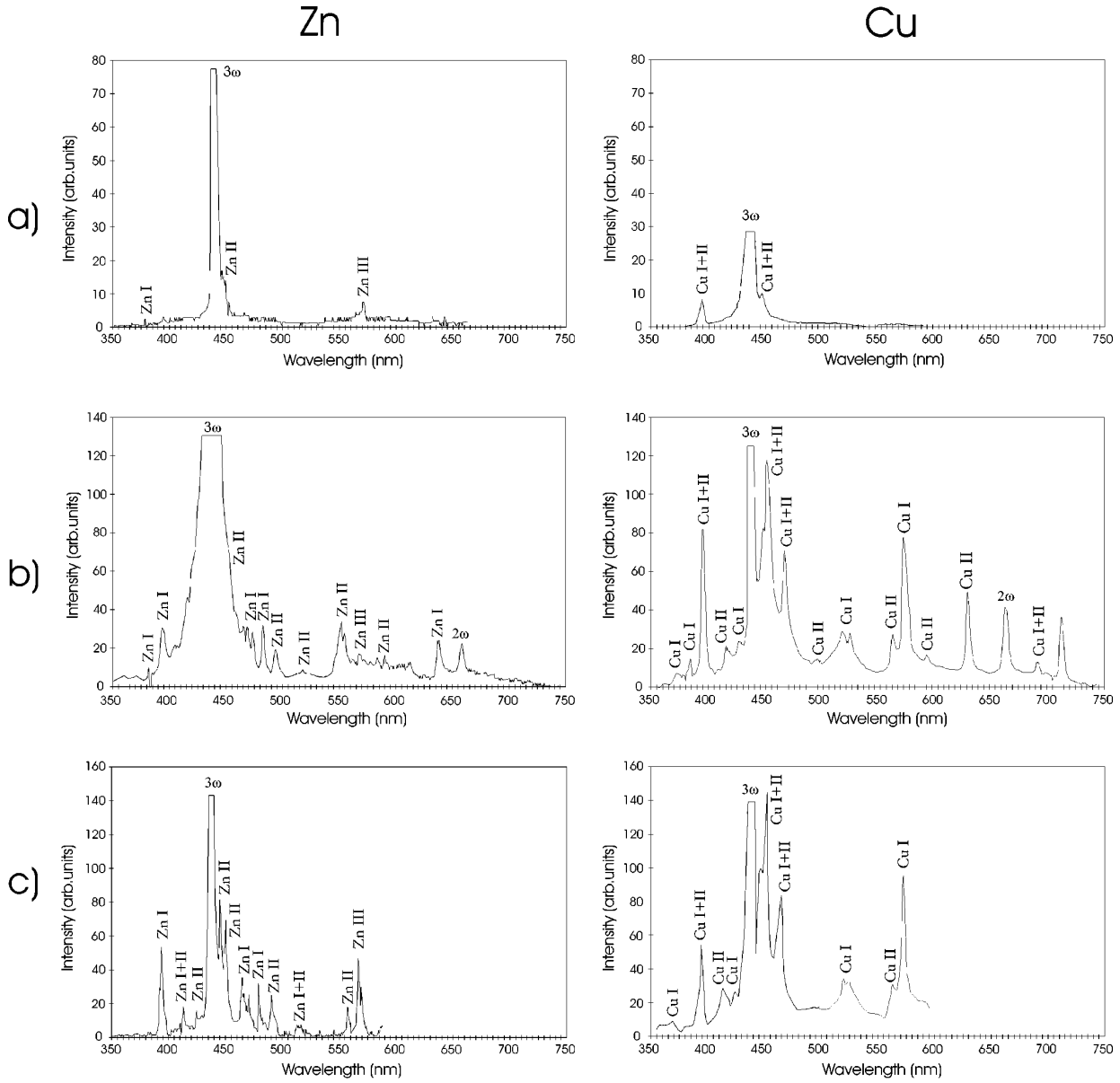

FIG. 5. The VIS-IR spectra produced by Zn and Cu plasmas driven by (a) 10^{10}, (b) 5×10^{10}, and (c) 10^{11} W cm^{-2}. The spectral resolution is $\sim$1 nm. The saturated peak near 438.3 nm corresponds to the 3ω interferometric probe; the second harmonic at 657.5 nm of laser emission may equally be seen in (b) and (c).

points at significant differences in the coupling to the solid surface of plasma energy.

B. VIS-IR spectroscopic measurements

A typical set of VIS-IR spectra of Zn and Cu plasmas driven by 10^{10}, 5×10^{10}, and 10^{11} W cm^{-2} is displayed in Fig. 5, where the wavelength-dependent throughput of the imaging optics and the spectral quantum efficiency of the CCD were used to correct the raw data. The spectral lines are identified according to Refs. [41,42], which also supply the atomic data necessary for evaluating T_e. Regarding the resolution of $\sim$1 nm, some peaks in the recorded spectra in fact consist of an array of unresolved lines. In Eq. (4) the spontaneous emission factor g_iA_i belonging to a particular line ($i=1,2$) is then replaced by sum term $g_{i1}A_{i1}+g_{i2}A_{i2}+\cdots$, where the indices 1,2, . . . correspond to the individual indistinguishable lines in the spectral peak used for the analysis.

The spectra obtained at 10^{10} W cm^{-2}, Fig. 5(a), exhibit only several weak lines, apart from the probe beam that saturates the detector near 438.3 nm. Peaks corresponding to neutral and singly ionized states may be identified for both Zn and Cu, while the Zn spectrum exhibits also a feature belonging to doubly ionized state (Zn III). This suggests a possibly higher temperature of the Zn plasma, however, the character of the spectra does not make possible a temperature analysis.

An abundance of spectral lines belonging to neutral and singly ionized states appears as the irradiance reaches 5×10^{10} W cm^{-2}, as seen from Figs. 5(b) and 5(c). The strongest features in the Zn spectra are Zn I $(3d^{10})4s8s\rightarrow4s4p$

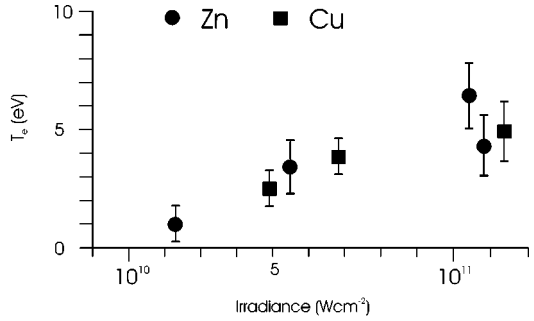

FIG. 6. The time- and space-integrated electron temperature of Zn and Cu plasmas as a function of the net laser irradiance. The values are relevant to the coronal plasma in late postpulse times (see text).

near 396.5 nm, Zn II $3d^{10}8d \rightarrow 3d^9 4s4p$ near 444.5 nm, and $3d^{10}7d \rightarrow 3d^9 4s4p$ near 450 nm, Zn I $3d^{10}4s5s \rightarrow 3d^{10}4s4p$ near 468 nm, and Zn II $(3d^{10})4f \rightarrow 4d$ near 491.2 nm. In addition, a spectral line near 568 nm, emerging strongly at 10^{11} W cm^{-2}, may be identified as stemming from a transition in the doubly ionized state Zn III $(3d^9)5p \rightarrow 5s$. The Cu spectra are dominated by peaks belonging to blends Cu I $(3d^9)4d \rightarrow 4p$, Cu II $(3d^9)6d \rightarrow 5p$, and $(3d^9)4d \rightarrow 4p$ near 394.5 nm, Cu I $3d^9 4s5s \rightarrow 3d^9 4p$ and Cu II $(3d^9)7s \rightarrow 5p$ near 452 nm, and by ''pure'' lines Cu I $3d^{10}4p \rightarrow 3d^9 4s^2$ at 570 nm and Cu II $3d^9 5d \rightarrow 3d^8 4s4p$ near 626 nm. No feature attributable to the doubly ionized state appears in the Cu spectra, providing an indication of a lower temperature.

The dominance of lines belonging to neutral and singly ionized states in both the Zn and the Cu cases appears striking; however, due to the time integration the spectra are strongly weighted towards the late postpulse period, as illustrated in Sec. IV. As a consequence, the temperatures inferred from these spectra are to be considered as representative for the period of decaying cool plasma–hot gas.

Figure 6 displays the inferred electron temperature as a function of irradiance. The points in the graph represent the average of a set of values obtained with the help of various combinations of pairs of lines belonging to a given ionization state (spectral peaks corresponding to a blend of lines stemming from different ionization states were excluded from the analysis). It turns out that the T_e magnitudes are similar for both Zn and Cu—albeit the Zn plasmas yield somewhat higher values, amounting to ~ 6 eV at 10^{11} W cm^{-2}. We emphasize again that these values do not represent the peak temperature attained within the laser pulse.

C. Spatially resolved plasma emission profiles

An example of data obtained by the VIS-IR imaging is shown in Fig. 7. The displayed CCD records correspond to Zn and Cu plasmas driven by 10^{10} and 10^{11} W cm^{-2}; the parasite speckles appearing near the right end of the target and for 10^{10} W cm^{-2} saturating the CCD stem from diffuse reflection of the 438-nm probe beam.

The data reveal that the lateral emission profiles strongly depend on the irradiance. While for 10^{10} W cm^{-2} the profiles correspond in width to the 100-μm imprint of the laser beam, for high irradiances there is an additional ''ramp'' signal spread over several hundred μm sideways to the laser impact. Due to the observation parallax of 60° with respect to the target normal it is obvious that this emission cannot stem from the underdense blowoff plasma sampled by the interferometric probing (in such a case the signal would greatly extend beyond the outline of the right target edge), and that it is emitted by a layer located near the surface.

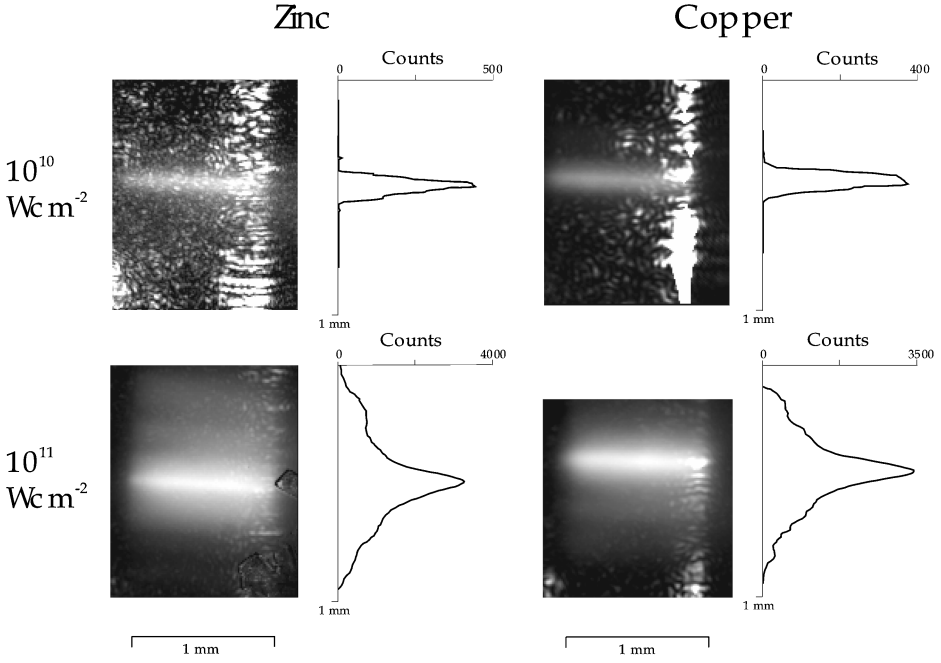

FIG. 7. Images of Zn and Cu plasma self-emission in the spectral region approximately 300–1100 nm (the parasite speckle patterns are due to the 438-nm interferometric beam coming from the right). The profiles plotted next to each record display the lateral distribution of the recorded emission (the 438 nm signal is eliminated).

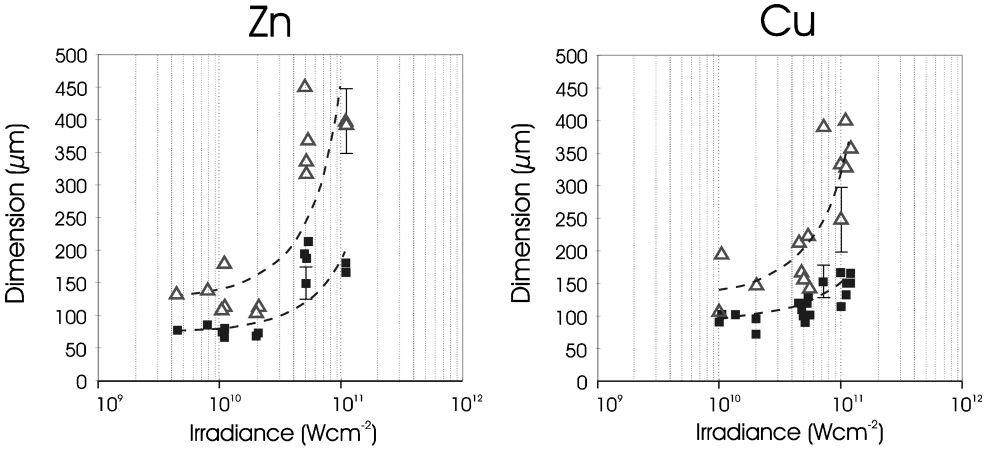

FIG. 8. Variation of the lateral size of the VIS-IR emission profiles with irradiance: the squares represent the full width at half maximum (FWHM) dimension, while the triangles indicate the width at 25% of the emission peak. The ''ramp'' emission sets on at lower irradiances for Zn ($\sim 5\times 10^{10}$ W cm^{-2}) than for Cu ($\sim 10^{11}$ W cm^{-2}), suggesting differences in lateral heat transport from the impact region to the target material and thereby in the crater formation.

The dependence of lateral features of the Zn and Cu emission profiles on irradiance is displayed in Fig. 8—the intensity distribution is characterized by the FWHM dimension, and by the width measured at 25% of the peak. These parameters are chosen as relevant respectively to the plasma directly heated by the laser and to the plasma producing the ramp signal. While the data display larger scatter than those obtained from the other two diagnostics, they clearly show that the emission profile characteristics are a stronger function of irradiance for Zn than for Cu. Both the FWHM of the central peak and the width of the ramp strongly rise at 5×10^{10} W cm^{-2} in the Zn plasmas, whereas Cu exhibits a more gradual increase of both signals, with a ramp extending to several hundred μm just at 10^{11} W cm^{-2}.

IV. DISCUSSION

The most informative experimental data are those supplied by the density probing. These provide two important pieces of evidence about the plasma evolution in the postpulse time. The first is that within the *whole* range of irradiances examined, the Zn and Cu plasmas evolve differently, producing different density profiles. The second is that when the laser pulse produces an irradiance exceeding a certain value specific to each element, the plasma develops into a pattern exhibiting symmetrical density flanks, which cannot be accounted for in the framework of a monodimensional flow model and by neglecting the material properties of the target. Both these observations conclusively show that material properties of the target are a substantial factor determining the postpulse plasma evolution, the nature of which is two dimensional in essence.

In examining reasons for the differences between the investigated plasmas, two issues have to be considered: the underlying effect may predominantly arise from different plasmas being created by the laser pulse, or alternatively as a result of different expansion histories of plasmas of initially similar parameters.

By using targets of different thermal properties, the generation of plasmas of different parameters may occur at weak irradiances, typically well below 10^{10} W cm^{-2}. While an accurate treatment of the interaction of the laser with a solid-density target requires numerical modeling, qualitative conclusions can be reached using a simple analytical approach [43]. This is based on the solution of the parabolic heat-flow equation for a semi-infinite solid of surface reflectivity R, irradiated by laser light, which is approximated to be deposited uniformly over the skin depth (cf. Table I). Considering a flat-top laser pulse of peak intensity I_0, linearly rising over time τ_r, the time necessary to heat the surface to a temperature T_S may be evaluated by

$$t \cong (3/2)^{3/2}\pi^{1/3}(KC\rho)^{1/3}\left(\frac{\tau_r}{(1-R)I_0}\right)^{2/3} T_S^{2/3}, \qquad (5a)$$

assuming that T_S is reached within the pulse rise time (i.e., if $t<\tau_r$), and by

$$t \cong \frac{\pi KC\rho}{(1-R)^2 I_0^2}\left(T_s + \frac{1}{3\sqrt{\pi}}\frac{(1-R)I_0}{\sqrt{KC\rho}}\,\tau_r^{1/2}\right)^2 \qquad (5b)$$

if T_S is attained at the peak of the pulse (i.e., if $t>\tau_r$); in both formulas K denotes the thermal conductivity, C the heat capacity, and ρ the mass density. It is important to note that while using a model based on simple heating of a solid and neglecting phase changes, Eqs. (5) may be adequately applied to assess the time necessary to bring the surface up to vaporization temperature. This is due to the fact that the energy spent in melting is of the order of ps and hence negligible compared to that consumed over the whole heating period. This may be shown using a simplified model [44] in which the time necessary to melt the skin depth δ is assessed as $\approx \tau_r \delta H((1-R)I_0 t_{\rm heat})^{-1}$, H being the latent heat of the phase transition and $t_{\rm heat}$ the time necessary to heat the surface to the temperature at which this change occurs.

Let us use Eqs. (5) to assess the time necessary to raise the surface temperature to the vaporization point, as a measure of the onset of plasma production for each target (while the ionization will likely proceed extremely quickly, having a character of a breakdown [45], its exact rate is rather difficult to estimate). Assuming $R=0.5$ as a reasonable estimate

for both targets, for a flat-top pulse of $\tau_r = 100$ ps producing $I_0 = 4 \times 10^9$ W cm^{-2}, vapor will be generated on the surface of a Zn target after ≈ 35 ps, while for Cu this will take ≈ 140 ps. Due to reduced thermal conductivity of both Zn and Cu liquid (cf. Table I) these numbers present a lower limit for the onset of generation of metal vapor—the ratio of the liquid conductivities is, however, comparable to that for the solid state, reinforcing the earlier development of the vapor in Zn.

The results obtained with the help of Eqs. (5) are displayed in Table II. It is apparent that below 10^{10} W cm^{-2} the time needed to heat the target before the plasma is produced is non-negligible with respect to the pulse duration. The different material properties of Zn and Cu will in turn lead to a larger amount of plasma produced from Zn targets. This indeed corroborates the experimental results, as seen from the $t = 4$ ns data shown in Figs. 3(a) and 3(b).

When the irradiance far exceeds 10^{10} W cm^{-2}, the time required to bring the surface to a vaporization point and hence to the onset of plasma generation progressively becomes negligible with respect to the total pulse duration. Material properties of the target are thus becoming insignificant—material is ablated and heated in the regime of high-temperature plasma, where the energy balance is controlled solely by the absorbed laser intensity near the critical surface, the diffusive electron heat conductivity, and the corona expansion velocity, which are similar for elements of neighboring Z. As a consequence, during the laser pulse action the interaction may be appropriately treated by a hydrodynamic model and material properties of the target may be disregarded. In other words, differences between the Zn and Cu plasmas may for these irradiances stem only from different postpulse evolution.

For the irradiance 10^{11} W cm^{-2}, we present a comparison of the measured electron density profiles (corresponding to the center of the focal spot) of Zn and Cu plasmas, and the profiles calculated by a 1.5D Lagrangian code EHYBRID [46,47]. This fully treats plasma hydrodynamics in the direction perpendicular to the target, while laterally its flow is assumed to be a self-similar isothermal expansion; the energy transport is modeled using flux limited ($f = 0.1$) Spitzer-Härm approach, and free electrons are assumed to behave as a nondegenerate perfect gas. The ionization kinetics is modeled through a modified Griem's model [47].

From Fig. 9 it is seen that for $t = 4$ ns the agreement between the calculated and the measured profiles is, over the region accessed experimentally, fairly good. The virtual identity of the calculated Zn and Cu profiles coincides with the observation that these profiles are similar to each other within the experimental error, although it should be noted that the data indicate the Zn plasma to exhibit a steeper profile (preventing probe beam penetration beyond ~ 100 μm) implying possibly higher densities close to the target. On the other hand, for $t = 10$ ns the predicted profiles do not account for the apparently different evolution of the Zn and Cu plasmas, underestimating the local density value in Zn while overestimating it in Cu.

Figure 10 illustrates calculated profiles of the electron temperature in a Zn plasma driven at 10^{11} W cm^{-2}, at 1-ns intervals after the pulse peak—the Cu profiles are nearly identical and are not shown, for the sake of clarity. The expanding corona is calculated to cool down to 10 eV in about 5 ns while further slowly falling over a tens-of-ns time scale, and the VIS-IR spectral measurement are hence strongly weighted towards late postpulse times.

From the comparison of the calculated and the actual density profiles it is clearly apparent that the target properties resume a role after the pulse is terminated, leading to plasma evolution increasingly element dependent with time elapsed since the laser pulse, and causing the 1.5D purely hydrodynamic treatment to progressively cease to be adequate for modeling the interaction. As a consequence, a realistic description should handle the problem in a fully 2D approach within which it has to deal in detail with heat dissipation

TABLE II. Time necessary to heat a solid target to vaporization temperature by a flat top laser pulse with a risetime of 100 ps, measured from the pulse onset [according to Eqs. (5)].

	Cu	Zn
Peak irradiance (W cm^{-2})	Time to vaporization (ps)	
4×10^9	36	138
10^{10}	19	65
5×10^{10}	7	23
10^{11}	4	14

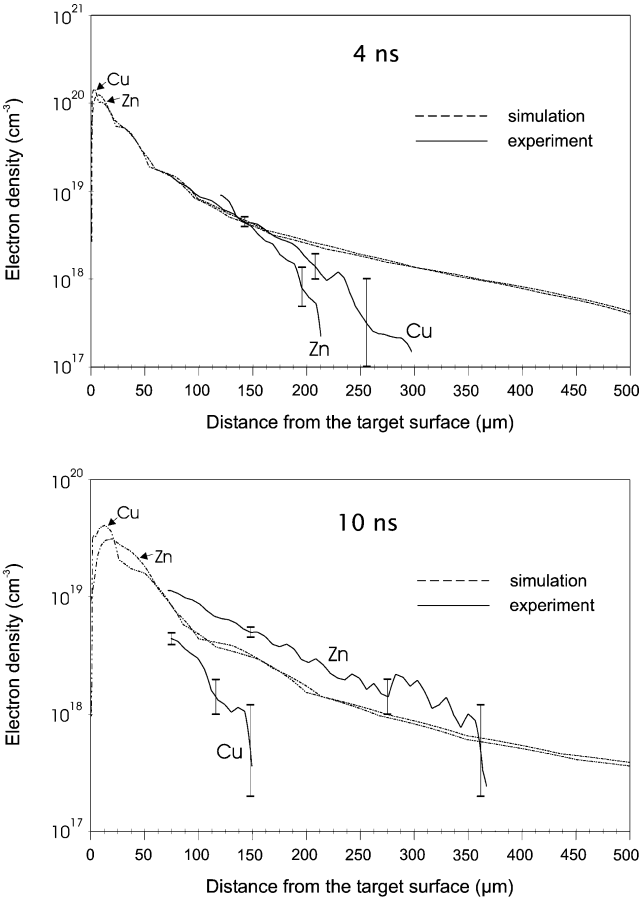

FIG. 9. The electron density profiles of Zn and Cu plasmas created by 10^{11} W cm^{-2}, in times 4 and 10 ns following the peak of the laser pulse. Dashed line: EHYBRID code predictions, solid line: experimental profiles (along a slice corresponding to the center of the laser focus).

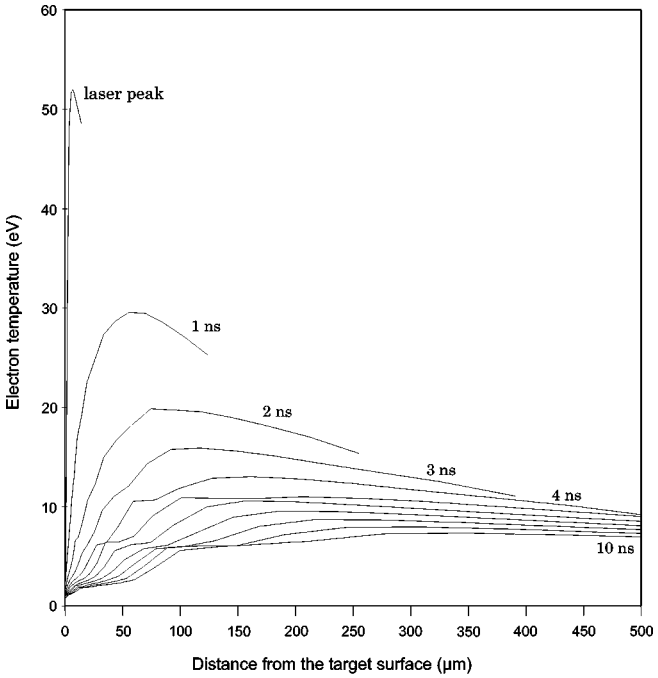

FIG. 10. Electron temperature profiles calculated by the EHYBRID code for a Zn plasma driven by 10^{11} W cm^{-2}, in times 0–10 ns relatively to the peak of the laser pulse, with increments of 1 ns.

from the plasma into the target and with low temperature ablation processes involved in the postpulse plasma generation.

The experimental data allow us to identify the principal effects responsible for the plasma behavior observed at the higher irradiances. As already noted, the density profile exhibiting the flank structure cannot be formed by free expansion of a plasma layer previously created by the laser pulse, but may be recognized as arising from a plasma additionally generated in the postpulse time and ejected under a given angle. The kinetics underlying this mechanism are presumed to be analogous to those involved in melt ejection arising in laser welding or hole drilling (e.g., [45]). To our knowledge, this work is the first to show such a phenomenon to occur in postpulse evolution of laser plasmas, although we note that it has been anticipated theoretically for the hot metal vapor regime at postpulse time scales of 100-ns order [48]. The principle is illustrated in Fig. 11. The plasma created by the laser pulse expands while producing heat flow and recoil pressure to the target. Depending on the rate at which the heat flow is dissipated by thermal conduction into the target material, the surface can be sustained to produce plasma well beyond the laser pulse. Due to the pressure exerted by the bulk plasma perpendicularly to the target and having a maximum in the center, this plasma will tend to run away in the lateral direction, and its flow will be liable to be controlled by the shape of the adjacent target surface. Thus, initially the flow will occur in the direction tangential to the target, while the gradually developing crater will progressively steer it to an angle with respect to the surface.

This scenario, which appears to be the only plausible one consistent with the experimental data, allows us to qualitatively understand the differences between Zn and Cu. Heat is dissipated more rapidly into the Cu target and more energy is

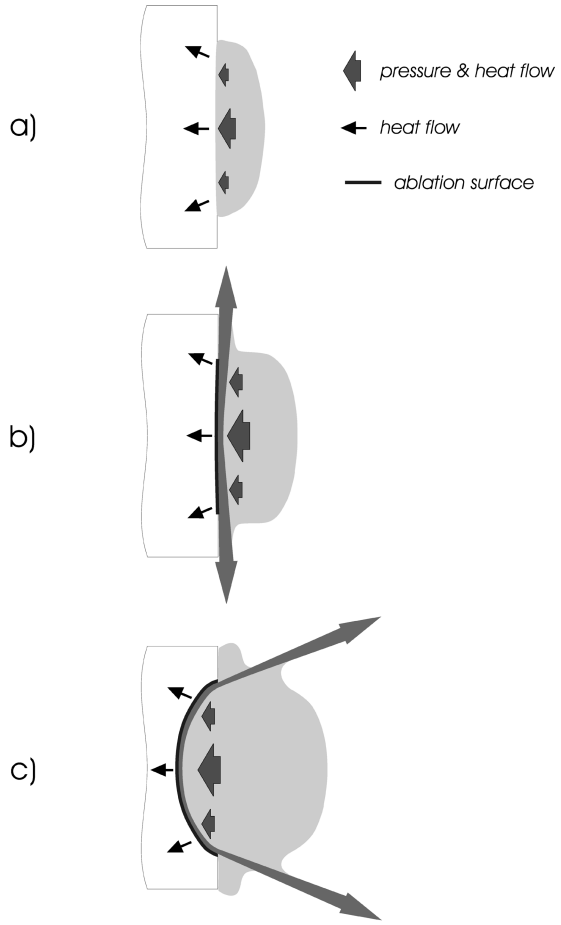

FIG. 11. Schematic of effects involved in the postpulse plasma evolution: the bulk plasma created by the laser acts as a heat sink capable of inducing further plasma generation in the postpulse period. (a) In case of a small amount of cool plasma and/or a material of high thermal conductivity the heat flow is matched by dissipation in the target and no postpulse plasma is generated. (b),(c) For an irradiance significantly in excess of 10^{10} W cm^{-2} and/or for a material of low thermal conductivity, the heat influx supplied maintains the conversion of the target surface to plasma subsequent to the pulse; a fraction of this plasma is first ejected sideways but is later steered by the crater to an angle, supplying the high-density flanks.

required to generate plasma, which will result in a smaller (or nonexistent) quantity of additional plasma and/or a higher cooling rate of the bulk plasma. The Cu plasmas at 10^{10} and 2×10^{10} W cm^{-2} thus merely decay in density, while in the case of Zn the heat flow is sufficient to generate the density flanks. For higher irradiances the energy influx from bulk plasma is large enough to generate additional plasma for both targets at early times, initially producing the spread-out surface layer (apparent in both the interferometric and the imagery data) while quickly forming a crater structure and supplying the flanks. The higher thermal conductivity of Cu is likely to give rise a larger plasma, which would explain the larger span between the density flanks compared to Zn, as seen in Figs. 3(d) and 3(e). On the other hand, the higher heat dissipation rate of Cu will cause termination of the plasma generation earlier than in Zn, as implied when comparing the $t=4$ and $t=10$ ns profiles in Figs. 3(d) and 3(e).

It should be noted that at higher intensities the data exhibit several surprising features, such as the filamentary streams in $t=4$ ns, shot-to-shot fluctuations of width of the dark region adjacent to the target and of the ''ramp'' signal of VIS-IR profiles, and a strongly pronounced flank structure for Cu in $t=4$ ns at 10^{11} W cm^{-2} compared to the corresponding Zn profile. Along with the basic observations made, they underline the complexity of the phenomena involved, which are poorly understood at present. These include most notably laser absorption in, and plasma generation from, a system liquid-vapor at a temperature beyond the critical point, ablation at low temperatures of the order of eV, heat transport issues such as electron and thermal conductivity in dense weakly ionized plasmas adjacent to solid and/or liquid state, effects of hydrodynamic flow pertinent to two-dimensional geometry, and so on. While some of these issues have recently been addressed or are currently being investigated [23,48–53], further experimental as well as theoretical effort is necessary to understand their role as an integral part of the interaction regime studied.

V. CONCLUSIONS

We have reported an investigation of Zn and Cu line plasmas created from slab targets irradiated by low-level laser pulses of intensity 4×10^{9} to 10^{11} W cm^{-2}, typical of the plasma created in the prepulse driving phase of sequentially pumped collisional x-ray lasers. We examined these plasmas by interferometric sampling and time-integrated VIS-IR spectroscopy and imaging. The data conclusively show that the Zn and Cu plasmas exhibit very different density profiles and expansion histories from one another. Furthermore, for irradiances in excess of 10^{10} W cm^{-2}, the exact value of which is strongly dependent upon the target material, a complex flow is established that exhibits a density profile with symmetric flanks and a central dip. We infer that the development of the plasma is strongly affected by energy dissipation effects and consequently depend on the solid state properties of the target material in question. The data suggest that the energy dissipation affects plasma evolution both during and after the laser pulse action. While below 10^{10} W cm^{-2} the heat flow into the target is the dominant factor in determining the energy balance of the laser-target interaction, for irradiances higher than 10^{10} W cm^{-2} it is only in the late phases of the expansion that the target properties are substantially involved in the plasma evolution.

We have compared the experimental density profiles for Zn and Cu plasmas created at an irradiance of 10^{11} W cm^{-2}, a regime in which the classical hydrodynamic approach should be appropriate during the pulse action, with 1.5D hydrodynamic calculations that neglect the material properties of the target. The predictions of theory and experimental observations diverge significantly at late plasma times. In particular, the profiles calculated do not match the substantially higher decay rate of Cu plasmas observed, which both ascertains the importance of target properties in the postpulse plasma evolution and points to the fundamentally 2D character of this evolution.

The results indicate that the plasmas created by prepulses are more complex than is generally assumed and explain the inadequacy of purely hydrodynamic 1.5D modeling to describe the action of a low-level prepulse. It is apparent that a deeper understanding of the postpulse dynamics of low-temperature laser plasmas is required, suggesting that the use of, e.g., soft x-ray interferometry to probe the dense plasma at the target surface would be productive. Furthermore, the development of 2D numerical models that treat the energy transport in some detail are essential for the accurate modeling of these systems.

ACKNOWLEDGMENTS

The authors thank L. Pina of the Czech Technical University for the loan of the high-resolution CCD cameras and for assistance in their implementation. We are indebted to J. Krasa of the Institute of Physics for help in calibrating the VIS-IR spectrometer, and to M. Hudecek, M. Soukup, J. Zeman, and J. Macha for providing technical support. Our thanks also go to Professor G. J. Pert of the University of York for making the EHYBRID code available to us. Finally, stimulating discussions with Phil B. Holden are greatly appreciated.

[1] *X-Ray Lasers 1994*, Proceedings of the 4th International Colloquium on X-Ray Lasers, edited by D. C. Eder and D. L. Matthews, AIP Conf. Proc. No. 332 (AIP, New York, 1994).

[2] *X-Ray Lasers 1996*, Proceedings of the 5th International Conference on X-Ray Lasers, edited by S. Svanberg and C.-G. Wahlström, IOP Conf. Proc. No. 151 (Institute of Physics, Bristol, 1996).

[3] J. Nilsen, B. J. MacGowan, L. B. DaSilva, and J. C. Moreno, Phys. Rev. A **48**, 4682 (1993).

[4] G. F. Cairns, M. J. Lamb, C. L. S. Lewis, A. G. MacPhee, D. Neely, P. Norreys, M. H. Key, C. Smith, S. B. Healy, P. B. Holden, G. Pert, and J. A. Plowes, in *X-Ray Lasers 1994* (Ref. [1]), pp. 289–292.

[5] B. Rus, A. Carillon, P. Dhez, B. Gauthé, P. Goedtkindt, P. Jaeglé, G. Jamelot, A. Klisnick, M. Nantel, A. Sureau, P. Zeitoun, *X-Ray Lasers 1994* (Ref. [1]), pp. 152–156.

[6] E. E. Fill, Y. Li, D. Schlögl, J. Steingruber, and J. Nilsen, Opt. Lett. **20**, 374 (1995).

[7] J. C. Moreno, J. Nilsen, and L. B. DaSilva, Opt. Commun. **110**, 585 (1994).

[8] H. Daido, R. Kodama, K. Murai, G. Yuan, M. Takagi, Y. Kato, I. W. Choi, and C. H. Nam, Opt. Lett. **20**, 61 (1995).

[9] S. Maxon, K. G. Estabrook, M. K. Prasad, A. L. Osterheld, R. A. London, and D. C. Eder, Phys. Rev. Lett. **70**, 2285 (1993).

[10] P. V. Nickles, M. Schnürer, M. P. Kalashnikov, I. Will, and W. Sander, Proc. SPIE **2520**, 373 (1995).

[11] J. Nilsen and J. C. Moreno, Phys. Rev. Lett. **74**, 2276 (1995).

[12] J. Zhang, P. J. Warwick, E. Wolfrum, M. H. Key, C. Danson, A. Demir, S. Healy, D. H. Kalantar, N. S. Kim, C. L. S. Lewis, J. Lin, A. G. MacPhee, D. Neely, J. Nilsen, G. J. Pert, R. Smith, G. J. Tallents, and J. S. Wark, Phys. Rev. A **54**, R4653 (1996).

[13] P. Jaeglé, A. Carillon, P. Dhez, P. Goedtkindt, G. Jamelot, A. Klisnick, B. Rus, P. Zeitoun, S. Jacquemot, D. Mazataud, A. Mens, and J. P. Chauvineau, in *X-Ray Lasers 1994* (Ref. [1]), pp. 25–34.
[14] B. Rus, A. Carillon, P. Dhez, P. Jaeglé, G. Jamelot, A. Klisnick, M. Nantel, and P. Zeitoun, Phys. Rev. A **55**, 3858 (1997).
[15] S. Sebban, P. Zeitoun, A. MacPhee, F. Albert, D. Benredjem, A. Carillon, P. Jaeglé, G. Jamelot, A. Klisnick, C. L. S. Lewis, M. Maillard, D. Ros, B. Rus, R. Smith, G. J. Tallents, L. Martin, A. M. Tournade, and P. Moreau (unpublished).
[16] J. Zhang, A. G. MacPhee, J. Nilsen, J. Lin, T. W. Barbee, Jr., C. Danson, M. H. Key, C. L. S. Lewis, D. Neely, R. M. N. O'Rourke, G. J. Pert, R. Smith, G. J. Tallents, J. S. Wark, and E. Wolfrum, Phys. Rev. Lett. **78**, 3856 (1997).
[17] Y. Li, G. Pretzler, and E. E. Fill, Phys. Rev. A , R2433 (1995).
[18] A. R. Präg, F. Loewenthal, and J. E. Balmer, Phys. Rev. A **54**, 4585 (1996).
[19] R. Kodama, H. Daido, K. Murai, G. Yuan, S. Ninomiya, Y. Kato, D. Neely, A. MacPhee, C. H. Nam, and I. W. Choi, Proc. SPIE **2520**, 25 (1995).
[20] J. Nilsen and J. C. Moreno, Opt. Lett. **20**, 1386 (1995).
[21] Y. Li, G. Pretzler, P. Lu, and E. E. Fill, Phys. Rev. A **53**, R652 (1996).
[22] J. A. Plowes, G. J. Pert, and P. B. Holden, Opt. Commun. **117**, 189 (1995).
[23] S. B. Healy, G. F. Cairns, C. L. S. Lewis, G. J. Pert, and J. A. Plowes, IEEE J. Sel. Top. Quantum Electron. **1**, 949 (1995).
[24] S. Jacquemot and L. Bonnet, Proc. SPIE **2520**, 169 (1995).
[25] G. J. Pert, S. B. Healy, J. A. Plowes, and P. A. Simms, in *X-Ray Lasers 1996* (Ref. [2]), pp. 528–532.
[26] M. Nantel, A. Klisnick, G. Jamelot, P. B. Holden, P. Jaeglé, P. Zeitoun, G. Tallents, A. G. MacPhee, and C. L. S. Lewis, Opt. Lett. **20**, 2333 (1995).
[27] G. Jamelot, P. Jaeglé, B. Rus, A. Carillon, A. Klisnick, M. Nantel, S. Sebban, F. Albert, P. Zeitoun, E. Plankl, A. Sirgand, C. L. S. Lewis, A. MacPhee, G. J. Tallents, J. Krishnan, and M. Holden, Proc. SPIE **2520**, 2 (1995).
[28] M. Nantel, A. Klisnick, G. Jamelot, P. B. Holden, B. Rus, A. Carillon, P. Jaeglé, P. Zeitoun, G. Tallents, A. G. MacPhee, C. L. S. Lewis, S. Jacquemot, and L. Bonnet, Phys. Rev. E **54**, 2852 (1996).
[29] G. F. Cairns, C. L. S. Lewis, M. J. Lamb, A. G. MacPhee, D. Neely, P. Norreys, M. H. Key, S. B. Healy, P. B. Holden, G. J. Pert, J. A. Plowes, G. J. Tallents, and A. Demir, Opt. Commun. **123**, 777 (1996).
[30] J. Nilsen, Y. Li, P. Lu, J. C. Moreno, and E. E. Fill, Opt. Commun. **124**, 287 (1996).
[31] G. Pretzler, K. Eidmann, and E. E. Fill, in *X-Ray Lasers 1996* (Ref. [2]), pp. 234–236.
[32] E. Wolfrum (private communication).
[33] D. C. Eder, P. Amendt, P. R. Bolton, G. Guethlein, R. A. London, M. D. Rosen, and S. C. Wilks, in *X-Ray Lasers 1992*, edited by E. E. Fill, IOP Conf. Proc. No. 125 (Institute of Physics, Bristol, 1992), pp. 177–184.
[34] A. G. MacPhee, C. L. S. Lewis, P. J. Warwick, I. Weaver, P. Jaeglé, A. Carillon, G. Jamelot, A. Klisnick, B. Rus, P. Zeitoun, M. Nantel, P. Goedtkindt, S. Sebban, G. J. Tallents, A. Demir, M. Holden, and J. Krishnan, Opt. Commun. **133**, 525 (1997).
[35] A. J. Moses, *The Practising Scientist's Handbook* (Van Nostrand Company, New York, 1978).
[36] *American Institute of Physics Handbook*, 3rd ed., edited by M. Zemansky (McGraw-Hill, New York, 1972).
[37] WebElements periodic table database, http://www.shef.ac.uk/-chem/web-elements/, M. Winter, Department of Chemistry, University of Sheffield, Sheffield S3 7HF, England (1996).
[38] T. Mocek, B. Rus, M. Kalal, P. Zeitoun, A. Demir, G. Jamelot, B. Kralikova, J. Krasa, L. Pina, S. Sebban, J. Skala, and G. J. Tallents, Proc. SPIE **2767**, 133 (1996).
[39] M. Kalal, B. Luther-Davies, and K. A. Nugent, J. Appl. Phys. **64**, 3845 (1988); see also M. Kalal, Czech. J. Phys. **41**, 743 (1991).
[40] C. De Michelis and M. Mattioli, Nucl. Fusion **21**, 677 (1981).
[41] W. L. Wiese, M. W. Smith, and B. M. Miles, Natl. Stand. Ref. Data Ser. **22** (1969).
[42] NIST Atomic Spectroscopic Database, http://aeldata.phy.nist.gov/, National Institute of Standards and Technology, Gaithersburg, MD 20899 (1996).
[43] B. Rus, Ph.D. thesis, Université Paris-Sud (unpublished).
[44] M. Sparks, J. Appl. Phys. **47**, 837 (1976).
[45] M. von Allmen, *Laser-Beam Interactions with Materials* (Springer-Verlag, Berlin, 1987).
[46] G. J. Pert, J. Fluid Mech. **131**, 401 (1983).
[47] P. B. Holden, S. B. Healy, M. T. M. Lightbody, G. J. Pert, J. A. Plowes, A. E. Kingston, E. Robertson, C. L. S. Lewis, D. Neely, J. Phys. B **27**, 341 (1994).
[48] T. Yabe, H. Daido, T. Aoki, E. Matsunaga, and K. Arisawa (unpublished).
[49] Y. T. Lee and R. M. More, Phys. Fluids **27**, 1273 (1984).
[50] H. M. Milchberg, R. R. Freeman, and S. C. Davey, Phys. Rev. Lett. **61**, 2364 (1988).
[51] A. N. Mostovych, K. J. Kearney, J. A. Stamper, and A. J. Schmitt, Phys. Rev. Lett. **66**, 612 (1991).
[52] G. R. Bennet, J. S. Wark, D. J. Heading, N. C. Woolsey, H. He, R. Cauble, R. W. Lee, and P. Young, Phys. Rev. E **50**, 3935 (1994).
[53] G. J. Pert (private communication).